Polarization-Resolved THz Imaging With Orthogonal Heterostructure Backward Diode Detectors

Yu Shi, Yijing Deng, Peizhao Li, *Graduate Student Member, IEEE*, Patrick Fay, *Fellow, IEEE*, and Lei Liu, *Senior Member, IEEE*

***Abstract*—A fully integrated lens-coupled dual-polarization detector for imaging was designed, fabricated, and characterized in the terahertz (THz) region. Two zero-bias heterostructure backward diodes were monolithically integrated into a planar dual-polarization annular-slot antenna. An impedance matching network consisting of an interdigitated dc block and shorted stubs was implemented for maximum power transfer. The fabricated chip was then mounted on an extended hemispherical silicon lens for high antenna efficiency. The performance of the integrated detector has been characterized at 200 GHz. The detector module can simultaneously measure the two orthogonal linear-polarized components of the incident THz waves, and hence obtain the polarization direction. On the basis of this polarimetric detection, polarization-resolved imaging of a Gaussian beam, as well as birefringent samples, was performed using the integrated detectors. The angular resolution of the polarization detection has been demonstrated to be as small as 3°. The single-pixel detector demonstrated here is amenable to array applications for THz focal-plane arrays that will have a significant impact on a wide range of remote sensing, through-barrier imaging, and detection/identification applications.**

***Index Terms*—Backward diode, dual-polarization detector, polarization imaging, terahertz (THz) imaging.**

I. Introduction

TERAHERTZ (THz) imaging has gained increasing attention in both scientific and industrial fields for a range of applications, including surveillance screening, chemical detection, pharmaceutical imaging, and radio astronomy [1], [2], [3], [4], [5], [6]. Most current THz sensing and imaging systems sense only the amplitude and/or phase from a single polarization of the incident field. However, it has been experimentally demonstrated that important features in THz signals and images arise not only from sample absorption or scattering but also from polarization shifts due to birefringence, oblique incidence, and multiple scattering events [7], [8], [9], [10], [11], [12], [13]. Consequently, the ability to unambiguously resolve the polarization of THz signals is important to fully exploit the information available in the THz regime. Examples include recent observation of polarization effects in THz Hall effect measurements [10], resolving finer spatial detail at the edges of scene features [11], and the observation of enhanced contrast for skin and colon cancer detection [12], [13]. In addition, THz detection with dual polarization is also of great interest in next generation THz communication [14] as well as astronomical observations [15]. Despite the clear value of polarization-resolved imaging, progress has been limited due to practical challenges in efficiently resolving polarization at THz frequencies.

To address the above problem, in [7], [8], and [11], THz time-domain spectroscopy (TDS) systems that utilize electro-optic sampling were used for polarization imaging applications. Although this approach can result in systems with high sensitivity and imaging speed, femtosecond pulse lasers and precise path length control are required [16], which significantly increases the cost and complexity of the imaging system. In addition, THz-TDS systems are typically restricted to imaging thin specimens mounted in an ultraclean chamber, which limits their use to within lab environments [3], [6]. In addition to THz-TDS systems, detectors, such as superconductor–insulator–superconductor mixers [17], microwave kinetic inductance detectors [18], and SiGe heterostructure bipolar transistors (HBTs) [19], [20], have also been demonstrated with polarization-sensitive antennas and/or waveguides for polarization detection. While the first two detectors must operate in cryogenic condition, HBT-based approaches require additional biasing circuits that unavoidably increase the flicker noise as well as the cost and complexity of the imaging system. Additionally, they are generally limited to operation below 1 THz [19], [20].

As an alternative to these prior approaches, we propose and demonstrate a monolithically integrated dual-polarization detector using zero-bias heterostructure backward diodes (HBDs). The detector circuit for a single pixel is illustrated in Fig. 1(a). Two orthogonal detector channels are integrated with a dual-polarization annular-slot antenna (ASA), enabling polarization-sensitive detection. By simultaneously measuring the amplitude of the two orthogonally polarized components, one can obtain the polarization direction of the incident electromagnetic (EM) wave. It should be noted that the narrow bandwidth of ASA can be beneficial to achieve high spectrum resolution in THz frequency spectroscopy applications. HBDs have been experimentally demonstrated to offer superior performance in the millimeter-wave to terahertz region [i.e., high responsivity, low

Manuscript received 21 November 2022; revised 18 January 2023; accepted 23 January 2023. Date of publication 3 February 2023; date of current version 3 May 2023. This work was supported by National Science Foundation under Grants ECCS-1508057, ECCS-1711631, ECCS-1711052, and ECCS-2223949. *(Corresponding author: Yu Shi.)*

The authors are with the Department of Electrical Engineering, University of Notre Dame, Notre Dame, IN 46556 USA (e-mail: yshi5@nd.edu; ydeng2@nd.edu; pli8@nd.edu; pfay@nd.edu; lliu3@nd.edu).

Color versions of one or more figures in this article are available at https://doi.org/10.1109/TTHZ.2023.3242230.

Digital Object Identifier 10.1109/TTHZ.2023.3242230

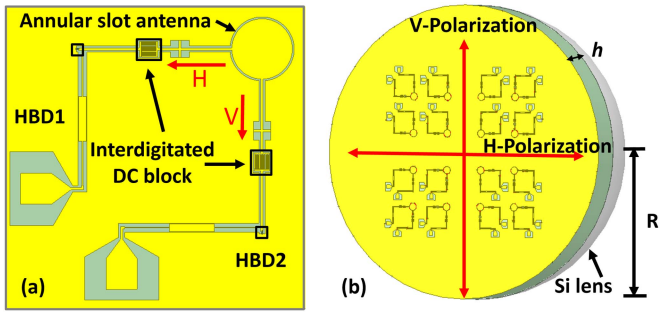

Fig. 1. (a) Schematic of the proposed polarization-resolved detector circuit. (b) Illustration of the lens-coupled FPA based on the proposed single-pixel detector for potential real-time polarization imaging applications.

noise equivalent power (NEP)] [21], [22], [23], [24]. Finally, as illustrated in Fig. 1(b), the proposed fully integrated detector is amenable to array applications for focal-plane arrays (FPAs) for high-performance real-time THz polarization imaging applications [25].

In this article, we extend our earlier work in [26] and present the detailed design, fabrication, and characterization of a prototype 200 GHz detector. We further verify the effectiveness of polarization imaging by using the detector in an imaging system, using it to resolve the polarization of a THz beam from a linear-polarized WR-5.1 horn antenna, as well as the demonstration of mapping the polarization shift due to the anisotropic dielectric properties of birefringent crystal samples. The polarization-resolved imaging angular resolution of the system is analyzed.

II. Detector Design

To demonstrate the concept experimentally, a single-pixel, dual-polarization detector was first designed for operation at 200 GHz and fabricated. As illustrated in Fig. 1(a), two detector channels, each consisting of a shorted-stub impedance matching network, interdigitated dc block, three-stage low-pass filters (LPFs), and an HBD, were integrated with a dual-polarization ASA. In order to achieve both high Gaussian coupling efficiency and high antenna directivity for THz operation, the detector chip was designed to be mounted on an extended hemispherical silicon lens [as illustrated Fig. 1(b)]. The detailed design for each component of the dual-polarization HBD detector is presented in the following sections.

A. ASA Design

Planar ASAs have been widely studied for dual-polarization operation. The port-to-port isolation can be as high as 25 dB [27]. The compact and symmetric geometry of the ASA makes it an attractive candidate to develop high-resolution imaging arrays [27], [28]. For the prototype reported here, the inner and outer radii of the ASA were 98 μm and 103 μm, respectively, for 200 GHz operation. The feeding coplanar waveguide (CPW) transmission line was designed to have a 7-μm-wide center conductor with 6.5-μm-wide gaps.

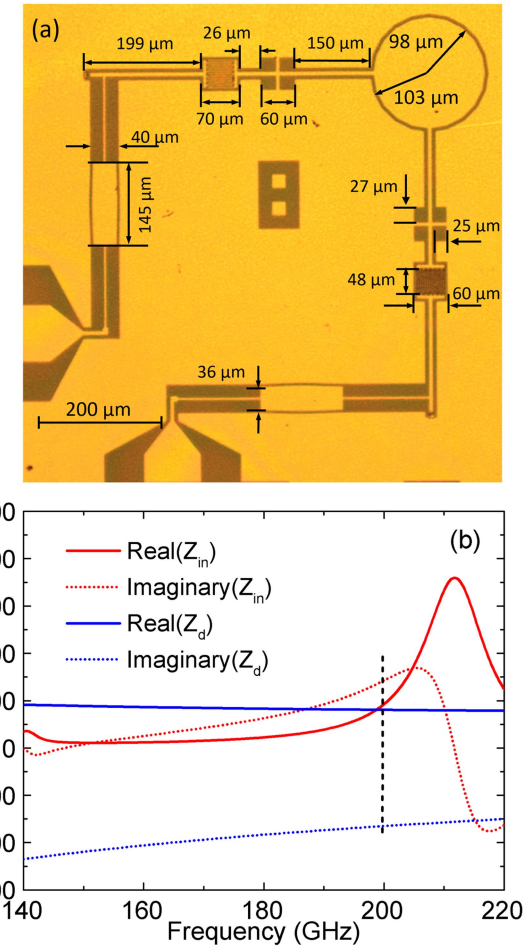

Fig. 2. (a) Optical microscope image of the detector circuit with designed parameters. (b) Intrinsic impedance of the HBD (Z_d) and the embedding impedance of the detector circuit (Z_{in}) from simulation. It can be seen that conjugate match has been achieved at 200 GHz.

B. Detector Circuit Design

To convert the dual-polarization signal at the ASA to baseband for processing, a two-channel detector circuit was designed. Each channel (one for horizontal (H) and vertical (V) polarizations, respectively) consists of a shorted-stub-based matching network, interdigitated dc blocking capacitor, and three-stage stepped-impedance LPF. A die photograph of the detector circuit with designed parameters is shown in Fig. 2(a).

Starting from the antenna feed port, a single-stub impedance matching network was designed to match the impedance of the HBD to that of the antenna. For this design, symmetric shorted stubs were added on both sides of the CPW transmission line to adjust the circuit admittance while supporting even mode propagation. For each shorted stub, the center conductor width was designed to be 6 μm, whereas the gap width was 27 μm. The length of each stub was 25 μm. The intrinsic impedance of the HBD from the device model [29], as well as the embedding impedance from full-wave simulation, is shown in Fig. 2(b). It can be seen that conjugate match has been achieved at around 200 GHz for narrow-band operation.

An interdigitated capacitor is used for the dc block to isolate the dc signals from the two orthogonal channels while minimizing the propagation loss at 200 GHz. In this design, a total number of 13 fingers was included. The width of each finger and gap was chosen to be 2 μm in accordance with the resolution of the optical lithography. The length of the finger was designed to be 48 μm. The interdigitated structure was simulated, and the insertion loss was found to be 1.95 dB at 200 GHz.

In order to extract the rectified dc outputs from the 200 GHz signal, a three-stage stepped-impedance LPF based on CPW transmission lines was used. In the LPF, each section was 145 μm long (i.e., quarter wavelength at 200 GHz) to place the 3 dB cutoff frequency at 88 GHz. For the low-impedance sections, the strip linewidth was 36 μm and the gap between the line and the ground was 2 μm wide, corresponding to a transmission line characteristic impedance of 23.3 Ω. For the high-impedance sections, the strip linewidth and the gap width were 2 μm and 19 μm, respectively. The characteristic impedance of the high-impedance section was 93.4 Ω from simulation. The insertion loss of the designed three-stage LPF was found to be 12.2 dB at 200 GHz in the same simulation.

C. Sb-Based HBD Design

Due to their high demonstrated sensitivity and low NEP, Sb-based HBDs were selected for the direct detector elements [23], [30]. Unlike Schottky barrier diodes [31] or other thermionic devices, the curvature coefficient of HBDs is not restricted by the q/kT limit so that larger sensitivity can be achieved. Prior demonstrations have shown zero-bias curvature coefficients as large as -58 V^{-1}, leading to a peak detector responsivity of $\sim$21000 V/W at 200 GHz [21].

In addition to large curvature coefficient and high responsivity, low NEP can also be achieved. As an important detector figure-of-merit, NEP quantifies the minimum input RF power that a detector can measure. For polarization detection applications, NEP determines the smallest power differences one detector channel can distinguish and, hence, determines the polarization angular resolution. According to the scalable device model and the prior measurements, the minimum NEP of the designed zero-bias HBD was experimentally demonstrated to be as low as 0.18 pW/$\sqrt{\text{Hz}}$ [23]. This level of NEP is achieved largely due to the extremely low $1/f$ noise due to operation without applied bias and enables detection in the THz regime without cryogenic cooling or preamplification. It should be noted that the $1/f$ noise increases at high signal level, as the rectified RF power will produce a small dc voltage (i.e., self-biasing). The dynamic range of the detector is, therefore, affected [32].

D. Quasi-Optical Design

In order to achieve high antenna directivity and Gaussian coupling efficiency for THz imaging applications, a quasi-optical configuration using an extended hemispherical silicon lens was employed [see Fig. 1(b)]. In this configuration, most of the transmitted rays that impinge on the silicon/air interface are refracted in the same direction, leading to a high-gain and high-efficiency radiation beam [33], [34], [35], [36]. For 2-D imaging arrays, this configuration can also reduce the crosstalk between the adjacent detectors by minimizing trapped surface waves within the substrate [35].

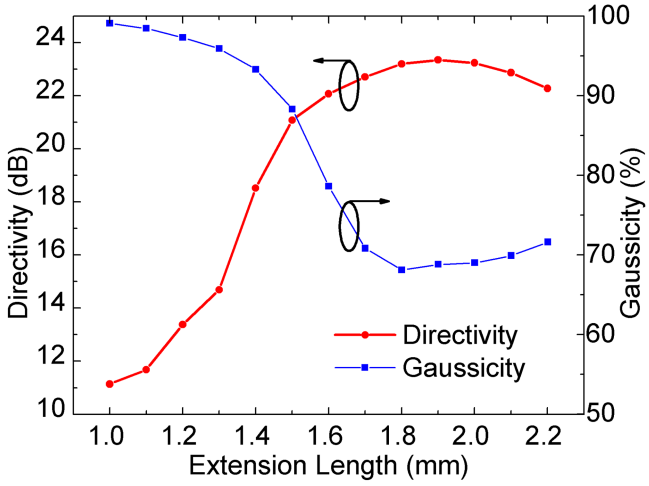

Fig. 3. Computed directivity and Gaussicity of the lens-coupled ASA with different extension lengths.

For the extended silicon lens used in this work, the radius (R) of 5 mm and the extension length (h) of 1.5 mm were chosen to achieve both high Gaussian coupling efficiency and good antenna directivity. On the basis of ray-tracing calculation [35], the lens-coupled ASA can provide a directivity of 21 dBi while maintaining a Gaussicity of approximately 88% at 200 GHz, as shown in Fig. 3. No antireflection coating layer was applied (reflection loss is estimated to be around 30%). If antireflection layer was provided on the Si lens, the directivity for operations at 200 GHz may be further improved [37], [38]. In addition, the Ohmic dissipation losses of the antenna was found to be around 0.9 dB in simulation. Therefore, the lens aperture efficiency was estimated to be 0.23.

III. Detector Fabrication

The fabrication of the proposed single-pixel detector follows the process flow described in [21]. The epitaxial layer structures were grown commercially by molecular beam epitaxy on a semi-insulating GaAs wafer. Electron-beam lithography was used to define the submicron-scaled active area (0.8 μm $\times$ 0.8 μm) of the two HBDs in the orthogonal channels, followed by the diode cathode contact deposition (Ti/Au/Ti) and lift-off. A self-aligned wet mesa etch process was used to fabricate the diode junction by selectively etching the InAs and Sb-bearing epitaxial layers.

Optical lithography and wet etching were then used to fabricate the bottom InAs isolation mesa. The isolation mesa area was 6 μm $\times$ 8 μm. In order to minimize the spreading resistance [21], a three-sided wrap-around Ti/Au (400-nm-thick) anode contact was deposited around the junction at a spacing of 700 nm. The planar ASA and other passive circuit elements, including the interdigitated dc blocks, LPF, and shorted stubs, were then deposited on the semi-insulating GaAs substrate. A

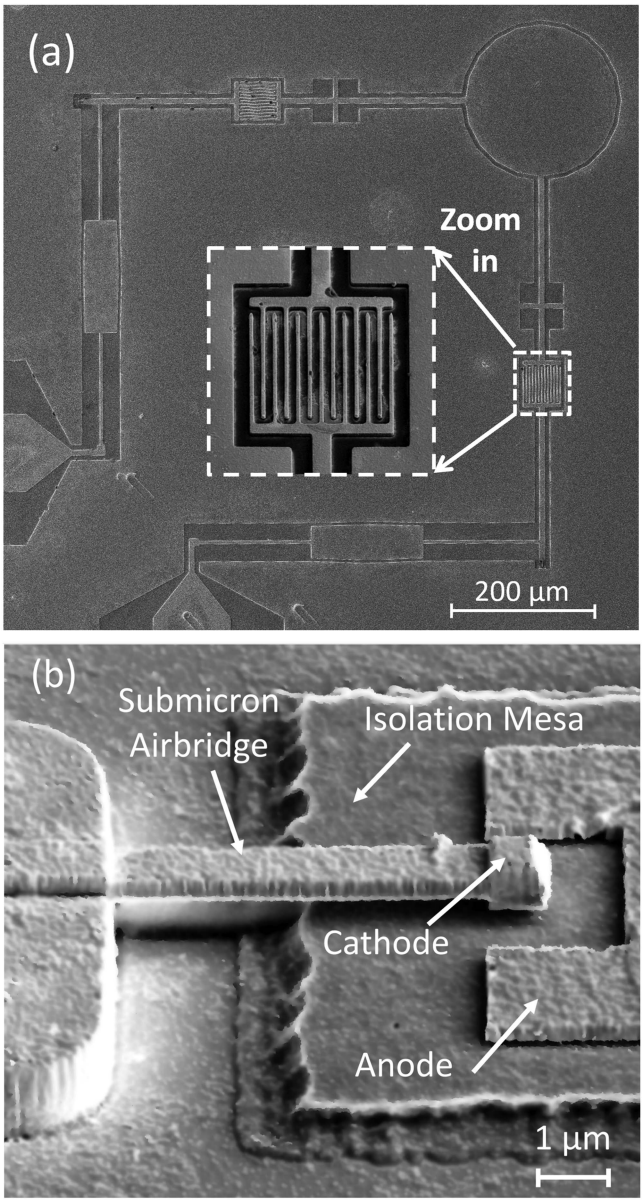

Fig. 4. SEM image of the (a) fabricated circuit and (b) HBD in V-channel.

benzocyclobutene (BCB) sacrificial layer was spin coated on the chip and then quasi-planarized through hard cure in N_2 environment. The cathode contact, as well as the passive circuit, was exposed after the BCB layer was thinned by blanket reactive ion etching. A total of 0.8-μm-wide airbridges were defined by electron-beam lithography, followed by 400-nm-thick metal (Ti/Au) deposition. The submicron-scaled airbridges were then released after the BCB sacrificial layer was removed using a high-pressure O_2/SF_6 dry etch. Finally, the detector chip was diced and mounted onto the silicon lens. An SEM image of the fabricated detector circuit as well as a close-up view of a completed HBD (from the horizontal channel) are shown in Fig. 4(a) and (b), respectively. It should be noted that the process employed here is robust and scalable to fabricating arrays of identical HBD detectors [21], [22].

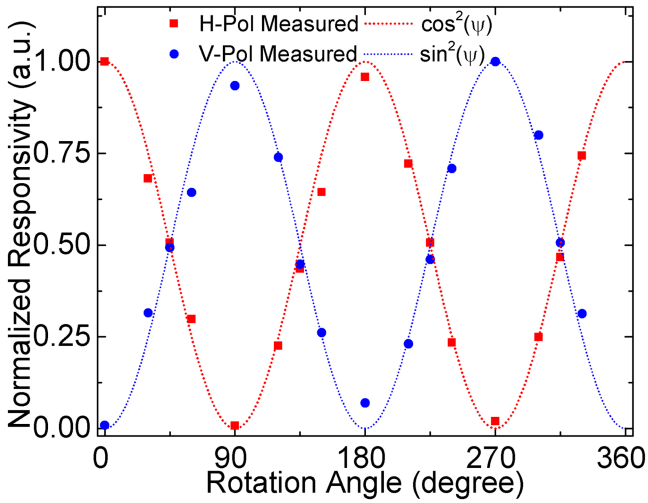

Fig. 5. Normalized responsivities (discrete points) under different rotation angles from H-polarization (H-Pol.) and V-polarization (V-Pol.) channel, respectively.

IV. Detector Characterization

A. Detection Testing

The dc and RF performance of the fabricated dual-polarization HBD detector was characterized before it was used as an imaging system. The responsivities of the two orthogonal channels at their individually aligned polarization were measured, and the peak values were found to be 115 V/W and 35 V/W for horizontal and vertical channels, respectively. The details about the measurement were presented in [26].

B. Polarization Detection

To assess the ability of the detector prototype to sense polarization, the dual-polarization detector was rotated (rotation angle ψ) along the polar axis of the silicon lens and the signal detected by each of the orthogonal channels was obtained. The measurement setup can be found in [26]. The normalized responses, as well as a unit-amplitude cosine-squared and a sine-squared function, are plotted in Fig. 5. From Fig. 5, one can see that the normalized response of the H-channel detector closely follows $\cos^2(\psi)$, while that of the V-channel follows $\sin^2(\psi)$. The cross-polarization coupling (η) between the two orthogonal channels was measured to be -21 dB. The results show that the two linearly polarized components of the incident EM wave can be individually detected by the corresponding orthogonal detector channel. Therefore, not only the intensity but also the polarization direction of the incident EM wave can be detected by the proposed integrated detector.

V. Polarization Imaging

A. Imaging of Gaussian Beam From Horn Antenna

In order to verify the effectiveness of polarization imaging using the integrated dual-polarization HBD detector, the transmitted THz beam from a WR-5.1 horn antenna was scanned to

form an image. The horn antenna under test was fed with an amplifier-multiplier chain (VDI-AMCS215b) and HP83712B synthesized generator. The integrated dual-polarization HBD detector was placed at a distance of 8 cm in front of the horn antenna to scan the radiated field at 200 GHz. The beam diameter in the imaging (scanning) plane was calculated to be 24.6 mm based on Gaussian beam transformation. The pixel size was 2 mm, and the entire imaging area was 4.0 cm × 4.0 cm (or 20 × 20 pixels). For each pixel, the outputs of the two orthogonal detector channels were simultaneously measured so that the intensity as well as the polarization direction can be obtained. Here, the total intensity I at each pixel was taken as the sum of the two intensities from the orthogonal channel measurements

$$I = I_{\mathrm{V}} + I_{\mathrm{H}} \tag{1}$$

and the polarization angle (PA) ψ was calculated from the ratio of those values

$$\psi \ = \tan^{-1}\left((I_{\mathrm{V}}/I_{\mathrm{H}})^{1/2}\right). \tag{2}$$

Images that include both normalized intensity (normalized to the peak intensity and represented by the color) and polarization direction (represented by the arrows) for the beam from 0°-rotated, 45°-rotated, and 90°-rotated single-polarized horn antenna are shown in Fig. 6. It can be seen from the intensity that a well-defined beam was observed in all three images. The main beam, whose diameter is 24.6 mm from calculation, is approximately represented as the rasterized circle (white) based on Bresenham's circle drawing algorithm with 12 mm radius [39]. The difference between the main beams in three intensity images is due to some minor misalignment and transmitting horn antenna being slightly tilted, especially for the 45°-rotation. The intensity measured at the pixels outside of the main beam was about 12–18 dB lower than that of the pixels within the beam. The signal level at those pixels that are far away from the main beam was, therefore, estimated to be around a few tens of nanowatt. The extracted PAs (arrows) at most pixels are consistent with the rotation angle. The discrepancies of the polarization measurements are likely due to the limited signal-to-noise ratio (SNR) at those pixels that are far away from the main beam with very low intensity.

In order to analyze and evaluate the polarization imaging performance, the mean value as well as the median, and the 25%–75% and the 2.5%–97.5% of the PAs were extracted and plotted in Fig. 7 for pixels within the estimated main beam. As can be seen, the extracted PA closely follows the rotation angle (i.e., 0°, 45°, and 90°). It can also be seen that, as compared with the results of the 45° measurement, the extracted PAs at a rotation of 0° and 90° are more consistent and less susceptible to noise as the deviation is relatively small. This is expected due to the sensitivity of (2) to finite SNR in I_{H} and I_{V}.

It is also worth pointing out that a ∼5° offset has been observed in both 0°- and 90°-rotated measurements. This is believed to be from the −21 dB cross-polarization coupling between the two orthogonal channels, which is also displayed in Fig. 5. This offset can be largely reduced by utilizing dual-polarization antennas of higher cross-polarization discrimination.

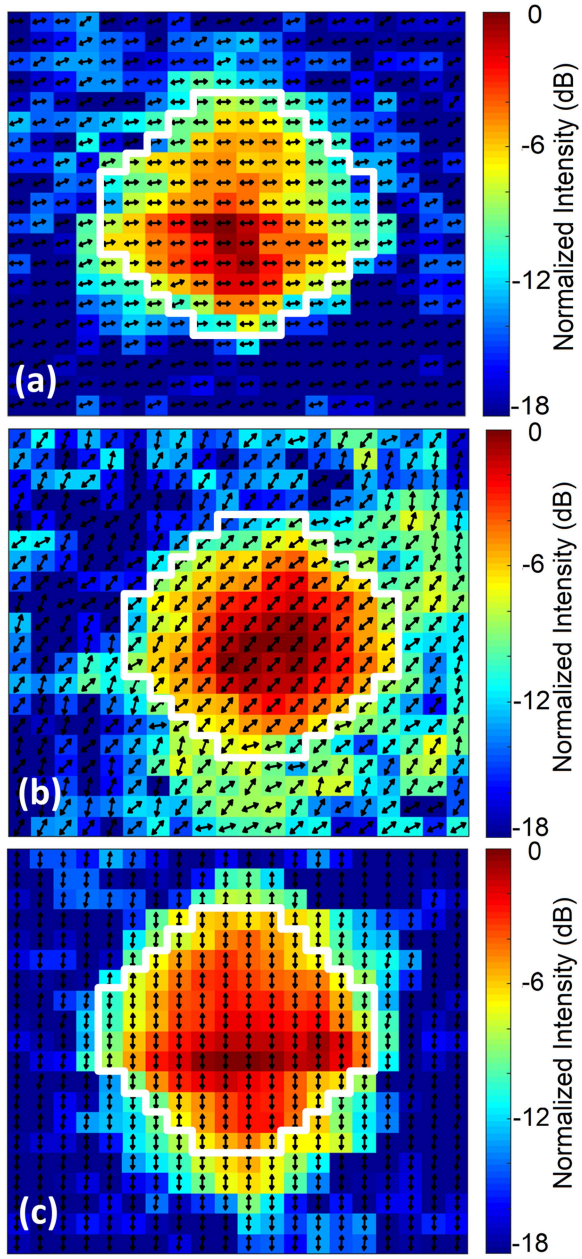

Fig. 6. Polarization imaging results of the beam from (a) 0°-rotated, (b) 45°-rotated, and (c) 90°-rotated single-polarized horn antenna. The normalized intensity is represented by the color and the polarization direction is represented by the arrow. The main beam is represented as the rasterized white circle from Bresenham's circle drawing algorithm with 12 mm radius.

The above polarization imaging results for the Gaussian beam from the rotated WR-5.1 horn antenna verify that the integrated dual-polarization detector can be used as a system for THz polarization imaging applications.

B. *Imaging of Birefringent Calcite Sample*

In order to further characterize and demonstrate the polarization imaging capability, the dual-polarization HBD detector was used to map the polarization shift introduced by birefringent crystal samples.

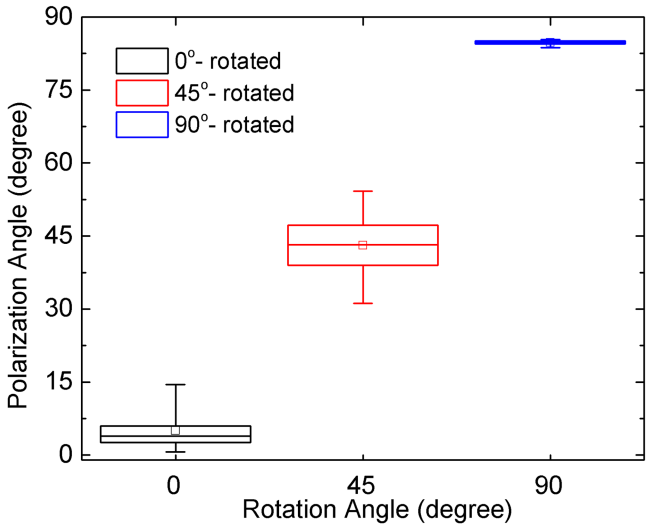

Fig. 7. Extracted PAs for the pixels in the main beam, when the rotation angle of the horn antenna is at 0°, 45°, or 90°. The line within the box is the median, the square is the mean value, the box represents the 25%–75%, and the error bar is the 2.5%–97.5% of observations.

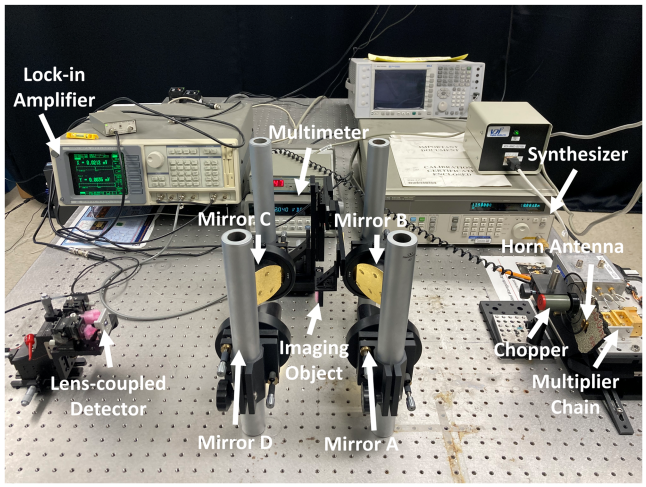

Fig. 8. Experimental setup for the polarization imaging measurement on birefringent calcite crystal.

For a birefringent crystal, the refractive indices of the ordinary and extraordinary wave (i.e., n_o and n_e) are different due to the anisotropic material property [8], [40]. For linear incident polarization, the THz wave is decomposed into ordinary and extraordinary wave components, and each experiences a different phase shift. As the phase difference between the two orthogonally polarized components changes, the transmitted wave will become elliptically polarized. This polarization change can be detected by the dual-polarization HBD detector, and an effective polarization angle (EPA) for describing the elliptical polarization can be measured.

The theoretical analysis of the polarization shift follows [40], [41], [42]. For a plane wave at normal incidence, if the electric field direction of the incident THz wave is aligned to the horizontal axis ($E_{\mathrm{H}}^{\mathrm{in}}$), the transmitted vertical ($E_{\mathrm{V}}^{\mathrm{out}}$) and horizontal ($E_{\mathrm{H}}^{\mathrm{out}}$) components can be obtained as follows:

$$E_{\mathrm{V}}^{\mathrm{out}} = E_o^{\mathrm{out}}\cos(\phi) - E_e^{\mathrm{out}}\sin(\phi) \tag{3}$$

$$E_{\mathrm{H}}^{\mathrm{out}} = E_o^{\mathrm{out}}\sin(\phi) + E_e^{\mathrm{out}}\cos(\phi) \tag{4}$$

where

$$E_o^{\mathrm{out}} = \frac{(1+\rho_o)(1-\rho_o)e^{-i\omega n_o L/c}}{1-\rho_o^2 e^{-i2\omega n_o L/c}} E_{\mathrm{H}}^{\mathrm{in}}\cos(\phi) \tag{5}$$

$$E_e^{\mathrm{out}} = \frac{(1+\rho_e)(1-\rho_e)e^{-i\omega n_e L/c}}{1-\rho_e^2 e^{-i2\omega n_e L/c}} E_{\mathrm{H}}^{\mathrm{in}}\sin(\phi) \tag{6}$$

$$\rho_{o(e)} = \frac{n_{o(e)}-1}{n_{o(e)}+1}. \tag{7}$$

Here, ω is the angular frequency of the incident THz wave, c is the speed of light, ϕ is the angle between the optical axis of the birefringent material and the horizontal axis, L is the thickness of the sample. E_o^{out} and E_e^{out} are the amplitudes of transmitted electrical field whose direction is along the ordinary and extraordinary axis of the birefringent crystal, respectively. ρ_o and ρ_e are the corresponding reflection coefficients for the ordinary and extraordinary wave at normal incidence. From (3) to (7), $E_{\mathrm{V}}^{\mathrm{out}}$ and $E_{\mathrm{H}}^{\mathrm{out}}$, and hence, the intensity of the transmitted wave with vertical and horizontal polarization direction (i.e., I_V and I_H), can be calculated. The intensities of the orthogonally polarized components can be measured by the dual-polarization HBD detector.

It should be noted that, because of the cross-polarization coupling (η) between each orthogonal channel, the measured intensity slightly deviates from the theoretical value, and an offset in EPA may be observed. The expected intensity from the orthogonal channels can be expressed as follows:

$$I_{\mathrm{V}}^{\mathrm{meas}} = (1-\eta)I_{\mathrm{V}}^{\mathrm{out}} + \eta I_{\mathrm{H}}^{\mathrm{out}} \tag{8}$$

$$I_{\mathrm{H}}^{\mathrm{meas}} = (1-\eta)I_{\mathrm{H}}^{\mathrm{out}} + \eta I_{\mathrm{V}}^{\mathrm{out}}. \tag{9}$$

The expected EPA (ψ_E) can be obtained from (2), the same equation as that for PA in Section V-A but with the deviated intensities from the measurements.

The measurement setup for the polarization imaging experiment is shown in Fig. 8. The 200 GHz incident wave was generated by a synthesizer (HP83712B) with a frequency multiplier chain (VDI-AMCS215b). The THz beam was transmitted through a horizontally polarized WR-5.1 horn antenna and modulated by the chopper in front. The modulated beam was then focused by a pair of 90° off-axis parabolic mirrors (i.e., Mirrors A and B in Fig. 8, focal length is 8.8 cm). The object being imaged was taped to a polystyrene foam holder and mounted on a 2-D motorized translation stage. It should be noted that the wavefront at the beam waist (i.e., focal point of the off-axis parabolic mirror) is flat so that the EM wave on the sample can be approximately treated as plane wave at normal incidence. The sample was scanned through the focused beam, whose diameter was estimated from Gaussian beam transformation to be 3 mm at the focus. The transmitted wave was then coupled

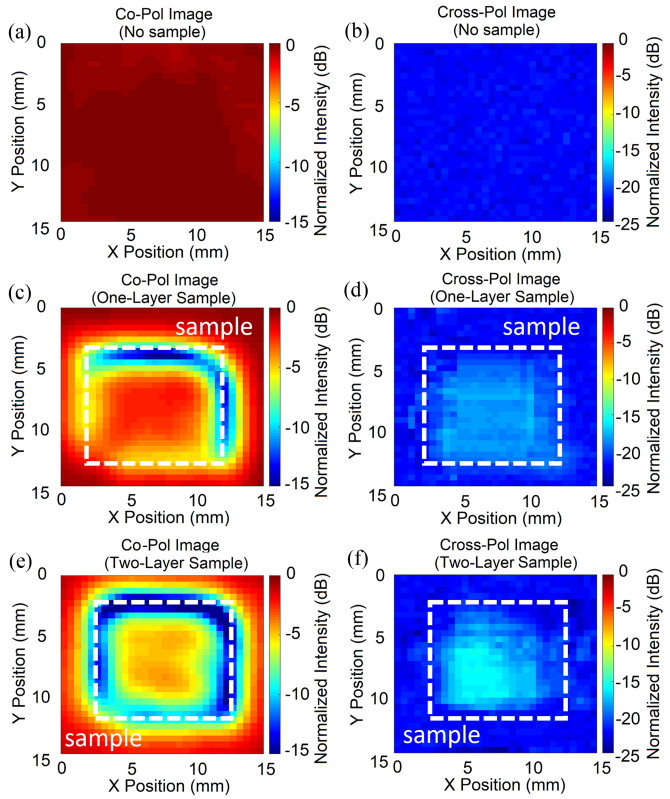

Fig. 9. Dual-polarization imaging results. (a) and (b) are the H-polarization and V-polarization imaging results with no sample. (c) and (d) are the imaging results of the one-layer calcite sample, whereas (e) and (f) are the corresponding images of the two-layer sample stack.

onto the integrated detector through a second pair of mirrors with the same parameters (i.e., Mirrors C and D). The dc signal of the integrated detector was measured by the lock-in amplifier (Stanford Research System SR850) and the digital multimeter (Agilent 34401A).

A selection of calcite crystals was chosen as the test objects due to calcite's significant difference in ordinary and extraordinary index in the THz region. The refractive index of the ordinary wave (n_o) in the calcite crystal is from 2.941 to 2.945 in the 0.15–0.3 THz range, whereas that of the extraordinary wave (n_e) is from 2.873 to 2.880 [43]. Due to the availability, only two 1.1-mm-thick calcite samples (from Karl Lambrecht Corp.) with an area of 10 mm $\times$ 10 mm were used in this test. The first imaging object was a single-layer calcite sample, whereas the second object consisted of two pieces in a stack. When the two pieces were stacked, the optical axis of the samples was aligned parallel so that the entire stack can be approximately treated as a single imaging object.

In this polarization imaging experiment, one-layer calcite sample and the two-layer stack were scanned through the focus of the THz beam. The incident wave was configured to be horizontally polarized, which corresponds to a 0° PA. The angle between the optical axis and the horizontal axis (ϕ) was set to be 45°, corresponding to the maximum achievable polarization shift [8]. The scanning step size was set to be 0.5 mm, and the total imaging area was 15 mm $\times$ 15 mm.

The dual-polarization imaging results obtained from the two orthogonal channels of the integrated detector are shown in Fig. 9. Fig. 9(a), (c), and (e) shows the H-polarization (which is also copolarization or Co-Pol) imaging results from the outputs of H-channel while scanning no sample, the one-layer calcite sample, and the two-layer stack, respectively. The intensity at each pixel in (c) and (e) was normalized to the measured "no sample" value in the H-channel measurement to compensate for any nonuniformity of the incident illumination. As can be seen in (c) and (e), a square object can be clearly seen in both images. The width of the edges is around 2.5 mm, which is primarily due to the relatively large beam spot size (which determines the spatial resolution) at 200 GHz. A much lower intensity can be observed at the edges because of scattering the incident wave off-axis. The average attenuation of the transmitted wave through the center of the calcite samples was measured to be 3.4 dB for the one-layer calcite and 5.6 dB for the two-layer stack. The measured attenuation is about 0.6 dB and 1.4 dB larger than the corresponding calculation result (2.8 dB and 4.2 dB), which is believed to be introduced by the calcite material loss at 200 GHz.

The corresponding V-polarization (cross-polarization or Cross-Pol) imaging results from scanning no sample, the one-layer calcite, and the two-layer stack are shown in Fig. 9(b), (d), and (f), respectively. For comparison, the measured intensities were again normalized to the same peak value as with the previous H-polarization measurement. When no sample was present, the average intensity at V-polarization [see Fig. 9(b)] was 22.1 dB lower than the peak value from H-polarization results, consistent with the cross-polarization coupling in Section IV-B. This can also be viewed as the noise floor of the V-polarization measurement. Similar to the images of the H-polarization, the calcite sample can also be observed in both Fig. 9(d) and (f) when there was imaging sample present. However, the normalized intensity of the transmitted wave increased from -18.5 to -17.5 dB when the sample thickness increased from 1.1 to 2.2 mm, clearly showing the impact of larger thickness on EPA rotation. The results slightly differ from the calculation results (-18.8 dB for one-layer calcite and -18.1 dB for two-layer stack), which is mainly due to the limited SNR, as well as the material loss mentioned above in H-polarization.

In addition, the EPA of the transmitted THz wave can be extracted based on the two orthogonal imaging results, as in (2). However, in order to capture the polarization shift from imaging object, an area selection algorithm was additionally developed. In this algorithm, only the pixel, whose intensity at V-polarization was at least 3 dB higher than the above-mentioned noise floor (i.e., SNR $>$ 1), while the intensity at H-polarization was lower than the result from no sample measurement, was selected as the calcite sample. For these pixels, the EPA was computed from the corresponding dual-polarization measurement results for the one-layer sample or the two-layer stack.

The polarization imaging results using the above algorithm for the one-layer sample and the two-layer stack are shown in

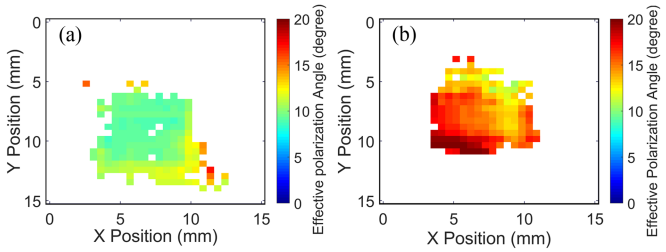

Fig. 10. Imaging results of the extracted EPA for (a) one-layer sample and (b) two-layer stack.

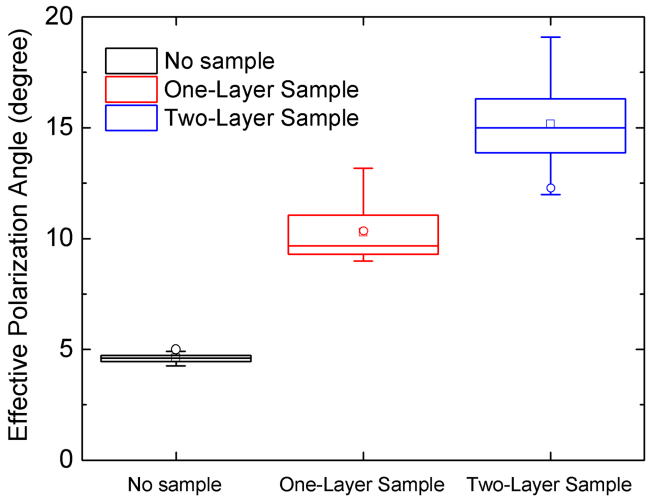

Fig. 11. Extracted EPA of the transmitted wave through no sample, one-layer, and two-layer sample area. The line within the box is the median, the square is the mean value, the box represents the 25%–75%, and the error bar is the 2.5%–97.5% of observations. The calculation results (circle), which has included the effects from the noise floor, are presented for comparison.

Fig. 10(a) and (b). It can be seen in both figures that the extracted EPA is reasonably uniform across the entire sample area. The deviation is likely due to the deviation during V-polarization measurement. As the thickness of the imaging object increased from 1.1 to 2.2 mm, the EPA of the transmitted THz wave increased from around 10° to 15°.

In order to quantitatively characterize the capability of the dual-polarization HBD detector as a polarization imaging system, in terms of angular resolution, the EPAs of the transmitted wave through different sample areas were statistically analyzed and shown in Fig. 11. The calculation results based on (3)–(9) are also plotted for comparison (circle). Similar to the previous 0°-rotated horn antenna measurement, a 4.6° offset can be observed when no sample is present, which is believed from the same cross-polarization coupling phenomenon. The median polarization shift introduced by the one-layer calcite is 9.7°, whereas that from the two-layer sample stack is 15.0°. It can be seen that the measurement results reasonably agree with the calculations in all three tests, showing the effectiveness of the dual-polarization detector as a polarization imaging system.

More importantly, the angular resolution of the polarization imaging system can be estimated from these measurements.

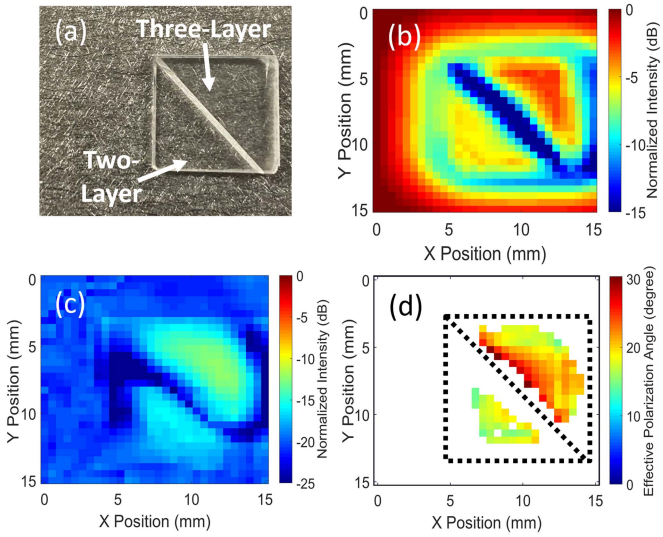

Fig. 12. (a) Photograph of the stacked triangle sample. (b) H-polarization image. (c) V-polarization image. (d) EPA image.

As shown in Fig. 11, the 25%–75% of the angular measurement on no-sample, one-layer calcite, and two-layer stack is 4.4°–4.7°, 9.3°–11.0°, and 13.9°–16.3°, respectively. Therefore, the minimum detectable change in the PA is estimated to be about 3°. It is worth mentioning that the angular resolution of the polarization imaging system could be further improved by utilizing HBDs with lower NEP and by employing antenna with better cross-polarization discrimination.

In addition to the simple stacked calcite samples, a relatively more complex imaging object with two different polarization regions was scanned by the same polarization imaging system to demonstrate its application. This imaging object consisted of a two-layer stacked square calcite as before and an additional piece of triangle calcite on top, as shown in Fig. 12(a). The two-layer and three-layer triangle regions were separated by the angled sidewall (cleavage plane) of the top sample. The optical axis of all three pieces was again aligned. The scanning step size, as well as the total imaging area, was kept the same as with the previous experiment.

Following the same procedures as discussed above, the dual-polarization imaging results from H- and V-channel detector have been obtained and shown in Fig. 12. Triangle objects can be clearly seen in both two-layer and three-layer area in the images.

The average attenuation of the transmitted wave through the center of the three-layer area was measured to be 4.5 dB from the H-channel detector, as shown in Fig. 12(b). The attenuation of the transmitted wave within the two-layer area is 5.9 dB. It is worth mentioning that the intensity of the transmitted wave through the three-layer stack is larger than that of the wave through the two-layer area. This is because of the combining impacts of the standing wave and the material birefringence, which is predicted from (3)–(9).

As shown from the V-polarization imaging results in Fig. 12(c), the normalized intensity measured within the three-layer area is −12.3 dB, whereas that of the two-layer area is −16.6 dB. This agrees with the earlier findings that larger thickness has a higher impact on EPA rotation.

On the basis of the dual-polarization imaging results, the EPA image of the sample was obtained and shown in Fig. 12(d). The EPA of the transmitted wave through the three-layer sample area (∼22°) is larger than that from the two-layer stack (∼16°).

In addition to EPA, the spatial resolution of the imaging system can be estimated from the dual-polarization images. As shown in both Fig. 12(b) and (c), the tips of the triangles in both images become rounded and blurry due to the limited spatial resolution associated with the spot size of the incident THz beam. By evaluating the minimal number of pixels for which the triangle tips are distinguishable, the spatial resolution can be approximately estimated to be ∼2.5 mm. This minimum detectable length is close to the beam size, consistent with the imaging system configuration.

VI. Discussion

Compared with the state-of-the-art THz-TDS system for polarization imaging applications, the imaging system that utilizes the fully integrated dual-polarization HBD detector is less complicated and more cost effective. The angular resolution of the polarization imaging system has been demonstrated to be around 3°, which is larger than that of the THz-TDS system [8]. However, it is still the first time, to the best of our knowledge, that the angular resolution of a polarization imaging system based on incoherent detector has been characterized.

More importantly, we believe that this angular resolution of the proposed polarization imaging approach using integrated dual-polarization HBD detector can still be significantly improved. The angular resolution of the polarization imaging system is fundamentally determined by the NEP and dynamic range of the HBD employed. Since the NEP of HBD has been experimentally demonstrated to be as low as 0.18 pW/$\sqrt{\text{Hz}}$ [23] (or theoretically 0.05 pW/$\sqrt{\text{Hz}}$ can be achieved [44]), the minimum detectable change from one channel is estimated to be 1.2 pW, assuming 50 Hz filter bandwidth. In addition, the maximum intensity that can be measured is approximately 0.93 μW from the previous dynamic range measurement [23], [29]. Therefore, we anticipate that the angular resolution by employing highly sensitive HBD can be potentially improved to be as high as 0.07°, which can exceed that of the THz-TDS system in [8]. It should be noted that the angular resolution of the polarization imaging system also depends on the systematic uncertainties, such as the cross-polarization coupling of the antenna. However, it is possible to switch to antenna with lower cross-polarization coupling, or perform postprocessing, to reduce system-level noise. The fundamental angular resolution limit is still determined by the performance of the HBD.

The proposed detector is scalable and can be readily modified and expanded to develop FPAs, which can significantly increase the imaging speed. In addition, the spatial resolution of the polarization-resolved imaging system can also be improved to be submillimeter by utilizing lens-coupled FPA. The resolution of the lens-coupled FPA is related to the spacing between the adjacent dual-polarization antenna. The dimension of the polarization-resolved detector unit cell is 900 μm × 900 μm. Therefore, the spacing between the adjacent ASA is approximately twice as long as the wavelength of the 200 GHz signal within silicon (i.e., $2\lambda_d$). The angular imaging resolution of the lens-coupled detector array is estimated to be around 9° based on the results in [45]. The resolution can be improved to 4° if the spacing between the adjacent ASA decreases to $0.8\lambda_d$ at the cost of reducing imaging contrast [45].

VII. Conclusion

In this article, a polarization-resolved single-pixel detector based on two orthogonally integrated HBDs has been demonstrated as a polarization imaging system in the THz region. The capability of the detector as a polarization imaging system has been demonstrated and quantitatively characterized, with angular resolution to be as high as 3°. The reported approach is promising for highly sensitive polarization imaging applications in remote detection, biomedical imaging, and radio astronomy.

Acknowledgment

The authors would like to thank the support from Advanced Diagnostics and Therapeutics Initiative (AD&T), Wireless Institution, and the Center for Nanoscience and Technology (ND-nano) at the University of Notre Dame, and the valuable assistance from the Virginia Diodes, Inc.

References

[1] D. M. Mittleman et al., "Recent advances in terahertz imaging," *Appl. Phys. B*, vol. 68, no. 6, pp. 1085–1094, 1999.
[2] K. Kawase, Y. Ogawa, Y. Watanabe, and H. Inoue, "Non-destructive terahertz imaging of illicit drugs using spectral fingerprints," *Opt. Express*, vol. 11, no. 20, pp. 2549–2554, 2003.
[3] P. Hillger, J. Grzyb, R. Jain, and U. R. Pfeiffer, "Terahertz imaging and sensing applications with silicon-based technologies," *IEEE Trans. Terahertz Sci. Technol.*, vol. 9, no. 1, pp. 1–19, Jan. 2019.
[4] The Event Horizon Telescope Collaboration et al., "First M87 event horizon telescope results—IV. Imaging the central supermassive black hole," *Astrophysical J. Lett.*, vol. 875, no. 1, 2019.
[5] D. M. Mittleman, "Twenty years of terahertz imaging," *Opt. Express*, vol. 26, no. 8, pp. 9417–9431, 2018.
[6] X. Zhang, T. Chang, Z. Wang, and H.-L. Cui, "Three-dimensional terahertz continuous wave imaging radar for nondestructive testing," *IEEE Access*, vol. 8, pp. 144259–144276, 2020.
[7] S. Watanabe, "Terahertz polarization imaging and its applications," *Photonics*, vol. 5, no. 4, 2018, Art. no. 58.
[8] X. Wang, Y. Cui, W. Sun, J. Ye, and Y. Zhang, "Terahertz polarization real-time imaging based on balanced electro-optic detection," *J. Opt. Soc. Amer. A*, vol. 27, pp. 2387–2393, 2010.
[9] J. Pearce, Z. Jian, and D. M. Mittleman, "Spectral shifts as a signature of the onset of diffusion of broadband terahertz pulses," *Opt. Lett.*, vol. 29, no. 24, pp. 2926–2928, 2004.
[10] D. M. Mittleman, J. Cunningham, M. C. Nuss, and M. Geva, "Noncontact semiconductor wafer characterization with the terahertz Hall effect," *Appl. Phys. Lett.*, vol. 71, no. 1, pp. 16–18, 1997.
[11] N. C. J. van der Valk, W. A. M. van der Marel, and P. C. M. Planken, "Terahertz polarization imaging," *Opt. Lett.*, vol. 30, pp. 2802–2804, 2005.
[12] R. M. Woodward et al., "Terahertz pulse imaging of ex vivo basal cell carcinoma," *J. Investig. Dermatol.*, vol. 120, no. 1, pp. 72–78, 2003.
[13] P. Doradla, K. Alavi, C. Joseph, and R. Giles, "Detection of colon cancer by continuous-wave terahertz polarization imaging technique," *J. Biomed. Opt.*, vol. 18, no. 9, 2013, Art. no. 090504.

[14] T. S. Rappaport et al., "Wireless communications and applications above 100 GHz: Opportunities and challenges for 6G and beyond," *IEEE Access*, vol. 7, pp. 78729–78757, 2019.
[15] T. Nakajima et al., "A new 100-GHz band front-end system with a waveguide-type dual-polarization sideband-separating SIS receiver for the NRO 45-m radio telescope," *Pub. Astron. Soc. Jpn.*, vol. 60, no. 3, pp. 435–443, 2008.
[16] J. Neu and C. A. Schmuttenmaer, "Tutorial: An introduction to terahertz time domain spectroscopy (THz-TDS)," *J. Appl. Phys.*, vol. 124, 2018, Art. no. 231101.
[17] K.-Y. Liu, M.-J. Wang, C.-T. Li, T.-J. Chen, and S.-C. Shi, "Development of a dual polarization SIS mixer with a planar orthomode transducer at 350 GHz," *IEEE Trans. Appl. Supercond.*, vol. 23, no. 3, Jun. 2013, Art. no. 1400705.
[18] B. Dober et al., "Optical demonstration of THz, dual-polarization sensitive microwave kinetic inductance detectors," *J. Low Temp. Phys.*, vol. 184, pp. 173–179, Jul. 2016.
[19] Z. Li et al., "A 0.32-THz SiGe imaging array with polarization diversity," *IEEE Trans. Terahertz Sci. Technol.*, vol. 8, no. 2, pp. 215–223, Mar. 2018.
[20] J. Grzyb, M. Andree, R. Jain, B. Heinemann, and U. R. Pfeiffer, "A lens-coupled on-chip antenna for dual-polarization SiGe HBT THz direct detector," *IEEE Antennas Wireless Propag. Lett.*, vol. 18, no. 11, pp. 2404–2408, Nov. 2019.
[21] S. M. Rahman, Z. Jiang, P. Fay, and L. Liu, "Integration and fabrication of high-performance Sb-based heterostructure backward diodes with submicron-scale airbridges for terahertz detection," *J. Vac. Sci. Technol. B*, vol. 34, no. 4, 2016, Art. no. 041220.
[22] S. M. Rahman, Z. Jiang, M. I. B. Shams, P. Fay, and L. Liu, "A G-band monolithically integrated quasi-optical zero-bias detector based on heterostructure backward diodes using submicrometer airbridges," *IEEE Trans. Microw. Theory Techn.*, vol. 66, no. 4, pp. 2010–2017, Apr. 2018.
[23] Z. Zhang, R. Rajavel, P. Deelman, and P. Fay, "Sub-micron area heterojunction backward diode millimeter-wave detectors with 0.18 pW/Hz$^{1/2}$ noise equivalent power," *IEEE Microw. Wireless Compon. Lett.*, vol. 21, no. 5, pp. 267–269, May 2011.
[24] D. J. Burdette et al., "Development of an 80 x 64 pixel, broadband, real-time THz imager," in *Proc. SPIE Terahertz Phys., Devices, Syst. V, Adv. Appl. Ind. Defense*, 2011, pp. 95–106.
[25] G. C. Trichopoulos, H. L. Mosbacker, D. Burdette, and K. Sertel, "A broadband focal plane array camera for real-time THz imaging applications," *IEEE Trans. Antennas Propag.*, vol. 61, no. 4, pp. 1733–1740, Apr. 2013.
[26] Y. Shi, Y. Deng, P. Li, P. Fay, and L. Liu, "A 200 GHz fully integrated, polarization-resolved quasi-optical detector using zero-bias heterostructure backward diodes," *IEEE Microw. Wireless Compon. Lett.*, vol. 32, no. 7, pp. 891–894, Jul. 2022.
[27] S. Raman and G. M. Rebeiz, "Single- and dual-polarized millimeter-wave slot-ring antennas," *IEEE Trans. Antennas Propag.*, vol. 44, no. 11, pp. 1438–1444, Nov. 1996.
[28] C. E. Tong and R. Blundell, "An annular slot antenna on a dielectric half-space," *IEEE Trans. Antennas Propag.*, vol. 42, no. 7, pp. 967–974, Jul. 1994.
[29] Z. Zhang, "Sb-heterojunction backward diodes for direct detection and passive millimeter-wave imaging," Ph.D. dissertation, Dept. Elect. Eng., Univ. Notre Dame, Notre Dame, IN, USA, 2011.
[30] J. N. Schulman et al., "W-band direct detection circuit performance with Sb-heterostructure diodes," *IEEE Microw. Wireless Compon. Lett.,* vol. 14, no. 7, pp. 316–318, Jul. 2004.
[31] L. Liu, J. L. Hesler, H. Xu, A. W. Lichtenberger, and R. M. Weikle, "A broadband quasi-optical terahertz detector utilizing a zero bias Schottky diode," *IEEE Microw. Wireless Compon. Lett.*, vol. 20, no. 9, pp. 504–506, Sep. 2010.
[32] A. Luukanen, E. Grossman, H. P. Moyer, and J. N. Schulman, "Noise and THz rectification characteristics of zero-bias quantum tunneling Sb-heterostructure diodes," *Int. J. High-Speed Electron. Syst.*, vol. 14, no. 4, pp. 921–939, 2004.
[33] S. Rahman, Z. Jiang, H. G. Xing, P. Fay, and L. Liu, "Lens-coupled folded-dipole antennas for terahertz detection and imaging," *IET Microw., Antennas Propag.*, vol. 9, no. 11, pp. 1213–1220, 2015.
[34] A. V. Boriskin, G. Godi, R. Sauleau, and A. I. Nosich, "Small hemielliptic dielectric lens antenna analysis in 2-D: Boundary integral equations versus geometrical and physical optics," *IEEE Trans. Antennas Propag.*, vol. 56, no. 2, pp. 485–492, Feb. 2008.
[35] D. F. Filipovic, S. S. Gearhart, and G. M. Rebeiz, "Double-slot antennas on extended hemispherical and elliptical silicon dielectric lenses," *IEEE Trans. Microw. Theory Techn.*, vol. 41, no. 10, pp. 1738–1749, Oct. 1993.
[36] A. Neto, S. Maci, and P. J. I. de Maagt, "Reflections inside an elliptical dielectric lens antenna," *IEE Proc.-Microw. Antennas Propag.*, vol. 145, no. 3, pp. 243–247, Jun. 1998.
[37] B. Cai, H. Chen, G. Xu, H. Zhao, and O. Sugihara, "Ultra-broadband THz antireflective coating with polymer composites," *Polymers*, vol. 9, 2017, Art. no. 574.
[38] K. Young et al., "Broadband millimeter-wave anti-reflection coatings on silicon using pyramidal sub-wavelength structures," *J. Appl. Phys.*, vol. 121, no. 21, 2017, Art. no. 213103.
[39] J. E. Bresenham, *Fundamental Algorithms for Computer Graphics*. Berlin, Germany: Springer, 1985.
[40] C. Jördens et al., "Terahertz birefringence for orientation analysis," *Appl. Opt.*, vol. 48, pp. 2037–2044, 2009.
[41] M. Reid and R. Fedosejevs, "Terahertz birefringence and attenuation properties of wood and paper," *Appl. Opt.*, vol. 45, pp. 2766–2772, 2006.
[42] D. M. Pozar, *Microwave Engineering*, 4th ed. Hoboken, NJ, USA: Wiley, 2012.
[43] E. D. Palik, *Handbook of Optical Constants of Solids*. Amsterdam, The Netherlands: Elsevier, 1998.
[44] L. Liu, S. M. Rahman, Z. Jiang, W. Li, and P. Fay, "Advanced terahertz sensing and imaging systems based on integrated III-V interband tunneling devices," *Proc. IEEE*, vol. 105, no. 6, pp. 1020–1034, Jun. 2017.
[45] L. Liu et al., "Design, fabrication and characterization of a submillimeter-wave niobium HEB mixer imaging array based on the 'reverse-microscope' concept," *IEEE Trans. Appl. Supercond.*, vol. 17, no. 2, pp. 407–411, Jun. 2007.

Yu Shi received the B.S. and M.S. degrees in optical engineering from the Huazhong University of Science and Technology, Wuhan, China in 2010 and 2013, respectively. He is currently working toward the Ph.D. degree in electrical engineering with the University of Notre Dame, Notre Dame, IN, USA.

Yijing Deng is currently working toward the Ph.D. degree in electrical engineering with the University of Notre Dame, Notre Dame, IN, USA.

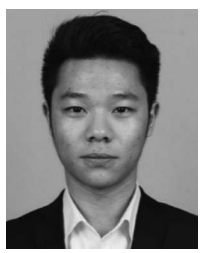

Peizhao Li (Graduate Student Member, IEEE) was born in Chengdu, China, in 1994. He received the B.S. degree in electronic information engineering from the Tianjin University of Technology, Tianjin, China, in 2017, and the M.S. degree in electrical engineering from Washington State University, Vancouver, WA, USA, in 2020. He is currently working toward the Ph.D. degree in electrical engineering with the University of Notre Dame, Notre Dame, IN, USA.

His research interests include mm-wave to THz circuits and systems (e.g., phased arrays, RF switches, and reconfigurable filters).

Patrick Fay (Fellow, IEEE) received the Ph.D. degree in electrical engineering from the University of Illinois at Urbana-Champaign, Champaign, IL, USA, in 1996.

He is currently a Professor with the Department of Electrical Engineering, University of Notre Dame, Notre Dame, IN, USA. He established the High-Speed Circuits and Devices Laboratory, Notre Dame, and oversaw the design, construction, and commissioning of the 9000-ft2 class 100 cleanroom housed in Stinson–Remick Hall at Notre Dame. He has been serving as the Director of this facility, since 2003. He has authored/coauthored 11 book chapters and more than 300 articles in scientific journals and conference proceedings. His research interests include design, fabrication, and characterization of microwave- and millimeter-wave electronic devices and circuits, the use of micromachining techniques for the fabrication of RF through submillimeter-wave packaging, and power devices.

Dr. Fay is a Distinguished Lecturer of the IEEE Electron Devices Society.

Lei Liu (Senior Member, IEEE) received the B.S. and M.S. degrees from Nanjing University, Nanjing, China, in 1998 and 2001, respectively, and the Ph.D. degree from the University of Virginia, Charlottesville, VA, USA, in 2007, respectively, all in electrical engineering.

From 2007 to 2009, he was a Postdoctoral Research Associate with the Department of Electrical and Computer Engineering, University of Virginia. In 2009, he joined the University of Notre Dame, Notre Dame, IN, USA, where he is currently an Associate Professor of electrical engineering. He has authored or coauthored ∼150 journal and conference papers. His current research interests include advanced THz sensing and imaging, tunable and reconfigurable THz circuits and components, THz detectors and mixers, submillimeter-wave and THz device and circuit design, modeling, and testing, quasi-optical techniques, novel microwave materials and devices, superconducting electronics, microfabrication and processing.

Dr. Liu served as a Session Chair of the 2006 IEEE Applied Superconductivity Conference, a Session Co-Chair of the 2015, 2018, and 2022 IEEE MTT-S International Microwave Symposium (IMS), and a Student Paper Competition Judge of the 2011 and 2017 IEEE MTT-S IMS. He is now serving as a steering committee member of the 2024 MTT-S IMS (Washington, DC, USA). He was the recipient of the IEEE MTT-S THz Prize (IEEE TRANSACTIONS ON TERAHERTZ SCIENCE AND TECHNOLOGY Best Paper Award) in 2019. His students were the recipients of the 2012 IEEE Asia–Pacific Microwave Conference (Taiwan) Student Prize, the 2012 International Conference on Infrared, Millimeter and Terahertz Waves (Wollongong, Australia) Best Student Paper Award, the 2015 IEEE MTT-S Graduate Fellowship Award, and the 2019 MTT-S International Microwave Conference on 5G and Beyond Best Student Paper Award (first place).